

Neutralization of H^- near vicinal metal surfaces

Boyan Obreshkov and Uwe Thumm

James R. Macdonald Laboratory, Department of Physics, Kansas State University, Manhattan, Kansas 66506-2604, USA

(Received 3 March 2006; revised manuscript received 31 May 2006; published 19 July 2006)

We calculate the neutralization probability of H^- ions due to charge transfer in collisions with metal vicinal surfaces. We apply a statistical Thomas-Fermi model with gradient correction to the kinetic energy and a local density approximation for the exchange-correlation energy to compute the ground-state electronic structure of the surface. In comparison with calculations for flat surfaces, we find work-function changes, induced by the vicinal superstructure, in good agreement with published experimental and theoretical data. We evaluate the shift and width of the H^- affinity level resonance for fixed positions of the ion near the surface. For incident anions with a kinetic energy of 1 keV, the calculated ion-neutralization probabilities depend sensitively on the impact direction, point of closest approach of the trajectory, and the surface morphology. We find that the ion survival is more likely if the H^- ions approach the step from above, as compared to ions that approach a step from below under otherwise identical scattering conditions. In particular, the electron loss after reflection at a terrace of a monoatomically stepped Al surface is predicted to be resonantly enhanced if the ion approaches a step from below.

DOI: [10.1103/PhysRevA.74.012901](https://doi.org/10.1103/PhysRevA.74.012901)

PACS number(s): 79.20.Rf, 73.22.-f, 34.70.+e, 71.15.Mb

I. INTRODUCTION

Experiments on the scattering of H^- and F^- ions on metallic surfaces [1,2] reveal that resonant charge transfer between the projectile and the surface via electron tunneling is the dominant process, which determines the lifetime of the negative ion. Various theoretical models have been developed for calculating the shifts and widths of the projectile energy levels in front of flat metallic surfaces [3–7]. Good quantitative agreement with the experiment of Guillemot and Esaulov [2] for the neutralization of H^- ions on flat Ag(111) surfaces is achieved in calculations based on a realistic model potential for the interaction of the electron with the surface [1,7].

Most theoretical studies neglect effects related to the lateral corrugation of the surface potential. A theoretical method for calculating the shift and broadening of hydrogen levels near impurity-covered surfaces shows that electron tunneling rates are either increased for positively charged or decreased in the case of negatively charged impurities [8]. The detailed study of the effects related to the lateral variation of the surface potential on the ion-neutralization probabilities is stimulated by recent experiments with vicinal surfaces [9,10], where angle-resolved photoemission measurements revealed lateral electron confinement in between surface steps. This confinement effect is attributed to both the periodic step structure and a surface band gap, which prevents fast tunneling decay of the confined electrons into the bulk of the substrate. Experiments involving the neutralization of O^- on Ni surfaces and Ne^+ on CdS surfaces at kinetic energies above 1 keV [11,12] indicate that the observed anisotropy of scattered ion fractions is a result of variations in the electronic charge transfer rates that are caused by the lateral change in the surface-electronic structure.

In the present paper, we study the reflection and neutralization of H^- ions with incident kinetic energies of 1 keV on nanostructured metal surfaces. Even though our method applies to arbitrarily structured surfaces, as a first application, we consider the special case of vicinal surfaces. The motion

of the active electron in the potential field of the projectile-surface system is described by the Schrödinger equation, and the projectile is assumed to move classically. In jellium approximation we replace the charge density of the positive ionic cores by a smeared-out, uniform background charge distribution. The electronic density of the surface and bulk and the electron-surface interaction potential are calculated by numerically solving the nonlinear Schrödinger equation within the self-consistent Thomas-Fermi-von Weizsäcker (TFvW) model [13,14]. For projectile energies of the order of 1 keV and large angles of incidence, charge transfer occurs at short distances in front of the surface where, as compared to atomically flat surfaces, the effects of the step structure on the surface modify both the electron transfer dynamics and the motion of the projectile. In fixed-ion approximation, the width of the H^- affinity level resonance is obtained by direct numerical integration of the two-dimensional time-dependent Schrödinger equation, including the two degrees of freedom of the active electron in the collision plane. The H^- neutralization probability after reflection from the surface is calculated from these static widths within a rate-equation approach [15,16] for a set of model broken-straight-line trajectories of the projectile, including both electron capture from and electron loss to the substrate.

The plan of this paper is as follows. In Sec. II, we describe the theoretical details of the calculation. In Sec. III we discuss our numerical results for both flat and vicinal surfaces. Section IV contains our conclusions. Unless stated otherwise we use atomic units ($e = \hbar = m_e = 1$).

II. THEORETICAL FORMULATION

In this section we present our method for calculating the width of the H^- affinity level and the ion-neutralization probability in front of metal surfaces. In Sec. II A, we show how the effective electron-surface interaction potential is evaluated. In Sec. II B, we apply this model to vicinal surfaces. In Sec. II C, we obtain the projected density of states, charge-transfer rates, and ion-neutralization probabilities by numeri-

cal propagation of the time-dependent Schrödinger equation. Some details of the numerical method for evaluating the effective electron-surface interaction potential are given in the Appendix.

A. Effective potentials

The effective potential felt by the active electron,

$$V = V_{e-H} + V_{e-surf}, \quad (1)$$

contains the electron-surface interaction potential in the absence of the hydrogen core, V_{e-surf} , and the electron-hydrogen interaction potential, V_{e-H} . We neglect corrections to the surface potential due to the response of the surface to the perturbing field of the neutral core of the projectile. The potential of the hydrogen core is represented by a spherically symmetrical model potential [17]. The model potential has a screened short-range Coulomb part and a long-range polarization part, which accounts for the interaction energy of the electron with the induced dipole moment in the hydrogen core,

$$U(r) = -(1/r)\exp(-2r) - (\alpha/2r^4)\exp(-\beta/r^2). \quad (2)$$

In this equation, r is the radial distance from the nucleus, $\alpha=9/2$ is the ground-state polarizability of hydrogen, and the parameter β is equal to 2.547. This potential holds a single weakly bound state with energy $E_a=-0.76$ eV. To ensure good numerical accuracy for small radial distances, the potential is regularized according to [18]

$$V_{e-H} = \frac{\gamma U}{\sqrt{\mu U^2 + 1}}. \quad (3)$$

We use a two-dimensional model to describe the ion-surface collision, in which the motion of the active electron is restricted to the collision plane of the projectile trajectory. To comply with the reduced dimensionality, the projectile-core potential is reparametrized [7] with values $\mu=0.1417$ and $\gamma=0.3923$, in order to yield the correct affinity (0.76 eV) of H^- .

The electron-surface interaction potential V_{e-surf} is calculated within the TFvW model for the equilibrium electronic density of metallic surfaces [13,14]. The ground-state energy density functional of the electron gas is

$$E[n] = T_s[n] + E_{xc}[n] + \frac{1}{2} \int d\mathbf{r} \int d\mathbf{r}' \frac{n(\mathbf{r})n(\mathbf{r}')}{|\mathbf{r} - \mathbf{r}'|} - \int d\mathbf{r} \int d\mathbf{r}' \frac{n_f(\mathbf{r})n(\mathbf{r}')}{|\mathbf{r} - \mathbf{r}'|}, \quad (4)$$

where $n(\mathbf{r})$ is the electronic density and $n_f(\mathbf{r})$ the density of the ionic cores in jellium approximation. The first term in Eq. (4) approximates the kinetic energy of a system of non-interacting electrons. We approximate this term as the sum of the Thomas-Fermi term and the leading nonlocal quantum correction to the kinetic energy (von Weizsäcker term),

$$T_s[n] = \int d\mathbf{r} \left[C_1 n^{5/3}(\mathbf{r}) + C_2 \frac{|\nabla n(\mathbf{r})|^2}{n(\mathbf{r})} \right]. \quad (5)$$

The coefficients are

TABLE I. Wigner-Seitz radius r_s , bulk electron density n_b , Thomas-Fermi screening length l_{TF} , and Fermi wavelength λ_F for some metals. All quantities are in a.u.

Metal	r_s	n_b	l_{TF}	λ_F
Al	2	0.0298	0.90	6.55
Cu	3	0.0088	1.11	9.82
Na	4	0.0037	1.28	13.10
K	5	0.0019	1.43	16.37

$$C_1 = \frac{3}{10}(3\pi^2)^{2/3}, \quad C_2 = \frac{\lambda_w}{8}. \quad (6)$$

Following the semiclassical expansion of the kinetic energy of the free-electron gas [19], the gradient parameter λ_w takes the value 1/9. This value is a valid approximation for a weakly inhomogeneous and weakly interacting electron gas. However, according to [14] the value $\lambda_w=1/4$ provides better quantitative agreement with density functional theory (DFT) calculations based on the Kohn-Sham approach [20] and will therefore be used in our numerical applications.

We adopt the local density approximation (LDA) for the exchange-correlation energy,

$$E_{xc}[n] = \int d\mathbf{r} n(\mathbf{r}) [\varepsilon_x(n) + \varepsilon_c(n)], \quad (7)$$

where the Dirac exchange energy is given by

$$\varepsilon_x(n) = C_3 n^{1/3}(\mathbf{r}). \quad (8)$$

For the electron correlation energy we use Wigner interpolation formula

$$\varepsilon_c = \frac{C_4}{C_5 + r_s(n)}, \quad (9)$$

with coefficients

$$C_3 = -\frac{3}{4} \left(\frac{3}{\pi} \right)^{1/3}, \quad C_4 = -0.44, \quad C_5 = 7.8. \quad (10)$$

The Wigner-Seitz radius r_s in Eq. (9) is related to the bulk density of the electrons $n_b=3/4\pi r_s^3$. Values for r_s that apply to Al, Cu, Na, and K crystals are listed in Table I, together with the Thomas-Fermi screening length $l_{TF}=k_F/(12\pi n_b)^{1/2} \sim r_s^{1/2}$ and the Fermi wavelength $\lambda_F=2\pi/k_F \sim r_s$, where $k_F=(3\pi^2 n_b)^{1/3}$ is the Fermi momentum.

The ground-state properties of the system are obtained by minimizing the energy-density functional (4), subject to the constraint that the total number of electrons be conserved. This is expressed by the Euler-Lagrange equation

$$\frac{\delta E[n]}{\delta n(\mathbf{r})} - \mu = 0, \quad (11)$$

where the Lagrange multiplier μ corresponds to the chemical potential of the system. Evaluating the first variational derivative in Eq. (4) gives the following equation for the electron density,

$$\begin{aligned} & \frac{5}{3}C_1n^{2/3}(\mathbf{r}) + C_2\left[\frac{\nabla n(\mathbf{r})}{n(\mathbf{r})}\right]^2 - 2C_2\frac{\nabla^2 n(\mathbf{r})}{n(\mathbf{r})} + \frac{4}{3}C_3n^{1/3}(\mathbf{r}) \\ & + C_4\frac{C_5 + (4/3)r_s(n)}{[C_5 + r_s(n)]^2} + \phi(\mathbf{r}) - \mu = 0. \end{aligned} \quad (12)$$

The electrostatic Hartree potential $\phi(\mathbf{r})$ arises from the densities of the electrons and the jellium ionic background and satisfies Poisson's equation

$$\nabla^2\phi(\mathbf{r}) = -4\pi[n(\mathbf{r}) - n_f(\mathbf{r})]. \quad (13)$$

The chemical potential is determined by the requirement that the charge density $n(\mathbf{r})$ approach its homogeneous bulk limit n_b deep inside the metal and by requesting that the electrostatic potential vanish deep inside the vacuum, such that

$$\mu = \frac{5}{3}C_1n_b^{2/3} + \frac{4}{3}C_3n_b^{1/3} + C_4\frac{C_5 + (4/3)r_s}{(C_5 + r_s)^2} + \phi_b, \quad (14)$$

where ϕ_b is the bulk value of the electrostatic potential.

By making the substitution $n(\mathbf{r}) = \psi_w^2(\mathbf{r})$, Eq. (12) results in the nonlinear Schrödinger equation for the ground-state von Weizsäcker wave function,

$$-\frac{\lambda_w}{2}\nabla^2\psi_w(\mathbf{r}) + v_{\text{eff}}(\mathbf{r})\psi_w(\mathbf{r}) = \mu\psi_w(\mathbf{r}), \quad (15)$$

with an effective potential

$$\begin{aligned} v_{\text{eff}}(\mathbf{r}) = & \phi(\mathbf{r}) + \frac{5}{3}C_1\psi_w^{4/3}(\mathbf{r}) + \frac{4}{3}C_3\psi_w^{2/3}(\mathbf{r}) \\ & + C_4\psi_w^{2/3}(\mathbf{r})\frac{C_5\psi_w^{2/3}(\mathbf{r}) + (4/3)(3/4\pi)^{1/3}}{[C_5\psi_w^{2/3}(\mathbf{r}) + (3/4\pi)^{1/3}]^2}. \end{aligned} \quad (16)$$

The electron-surface interaction potential is evaluated as the sum of the electrostatic Hartree potential and the local density approximation for the effective exchange-correlation potential,

$$V_{e\text{-surf}}(\mathbf{r}) = \phi(\mathbf{r}) + \frac{\delta E_{\text{xc}}[n]}{\delta n(\mathbf{r})}. \quad (17)$$

B. Application to vicinal surfaces

In order to simulate nanostructured surfaces within the jellium model, the positive background charge density is periodically corrugated in the optical plane, following the surface superstructure. We choose a right-handed Cartesian laboratory reference frame S with origin situated on the step ledge at the middle between the upper and lower corners of the step (Fig. 1). The x and y axes are lying in the optical surface plane, and the z axis is directed along its outward normal. In order to determine the electronic charge density, we represent the superimposed surface structure by introducing the shape function $\xi(x, y)$ and assume that the uniform jellium background charge density $n_f(\mathbf{r})$ is confined to the space $z < \xi(x, y)$ —i.e., $n_f(\mathbf{r}) = n_b\theta(\xi(x, y) - z)$ where $\theta(x)$ is the Heaviside step function.

More specifically, for a periodically structured vicinal surface that is translationally invariant along the y axis, we in-

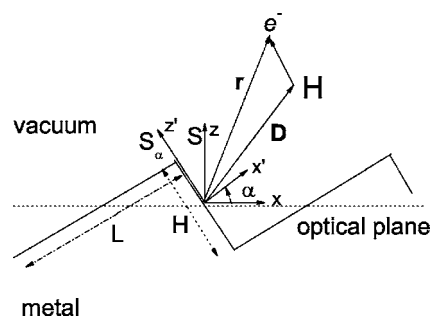


FIG. 1. Geometry and coordinate systems S and S_α for a vicinal surface with step length L , step height H , and a miscut angle α . The optical surface plane is indicated by the dotted line. \mathbf{D} is the position vector for the projectile and \mathbf{r} for the electron.

roduce a terrace width L and a step ledge of height H . The surface of the ledge is orthogonal to the surfaces of the two adjacent terraces. We chose the terrace to be $L = ma_0$ atoms wide and na_0 atoms high, where a_0 is the lattice spacing in the plane with (001) orientation. This configuration corresponds to the $[m(001) \times n(100)]$ structure, according to the notation in [21].

More suitable for the numerical calculation is the reference frame S_α , which is obtained by rotation $R_\alpha: \mathbf{r}' = (x', y', z') = R_\alpha \mathbf{r}$ of the frame S about its y axis by the miscut angle $\alpha = \arctan(H/L)$, such that the z' axis of the new reference frame is directed along the outward terrace normal. Both reference frames are shown in Fig. 1. The jellium profile function ξ in S_α is given by

$$\xi(x') = \frac{H}{2}[\theta(x') - \theta(-x')], \quad -L/2 \leq x' \leq L/2. \quad (18)$$

We have solved numerically the system of coupled equations (13) and (15) in the rectangular domain

$$\Omega = [-L/2, L/2] \times [-Z, Z] \quad (19)$$

in the reference frame S_α , subject to the boundary conditions

$$\mathbf{e}_{x'} \cdot \nabla \psi_w = 0, \quad \mathbf{e}_{x'} \cdot \nabla \phi = 0, \quad x' = \pm L/2, \quad \forall z' \in \Omega, \quad (20)$$

$$\psi_w(x', -Z) = \sqrt{n_b}, \quad \psi_w(x', Z) = 0, \quad \forall x' \in \Omega, \quad (21)$$

$$\mathbf{e}_{z'} \cdot \nabla \phi = 0, \quad z' = \pm Z, \quad \forall x' \in [-L/2, L/2], \quad (22)$$

where $\mathbf{e}_{x'}$ and $\mathbf{e}_{z'}$ are unit vectors directed parallel and perpendicular to the terrace, respectively. The end points $-Z$ and Z are chosen sufficiently far in the homogeneous bulk and vacuum ($Z \gg r_s$), respectively, that the solutions in the surface region are insensitive to variations of that range. The homogeneous Neumann boundary conditions (20) and (22) imposed on the electrostatic potential, together with the boundary conditions for the wave function, ensure charge neutrality of the jellium system in the domain Ω . The first set of conditions (20) explicitly assumes that in S_α the wave function and the electrostatic potential do not vary with the lateral coordinate x' across these boundaries. This is justified if the electron densities of two adjacent steps do not overlap

significantly. This means that the terrace period $L=ma_0$ needs to be larger than the Thomas-Fermi screening length $l_{\text{TF}} < a_0$, i.e., $m \gg 1$. The remaining set of boundary conditions in (21) and (22) is dictated by the homogeneity of bulk and vacuum.

The numerical solution for the electrostatic potential and the wave function are periodically replicated (in the S_α frame) in a larger domain $\mathcal{D} = \Omega \oplus \Omega \oplus \dots \oplus \Omega$, following the contour of the corrugated jellium profile. By construction, the numerical solution, together with its spatial gradient, is a continuous function in \mathcal{D} . The values of ψ_w and ϕ at some point $\mathbf{r}' \in \mathcal{D}$ are calculated by translation from points in the reference domain $\mathbf{r}'_0 \in \Omega$ along a vector $\mathbf{a} = (n_1 L, n_2 H)$, where n_1 and n_2 are integer numbers,

$$\psi_w(\mathbf{r}') = \psi_w(T_{\mathbf{a}}^{-1} \mathbf{r}'_0), \quad \phi(\mathbf{r}') = \phi(T_{\mathbf{a}}^{-1} \mathbf{r}'_0). \quad (23)$$

The wave function and the electrostatic potential are subsequently evaluated in the laboratory frame S by back rotation around the step edge direction by the miscut angle α ,

$$\psi_w(\mathbf{r}) \leftarrow \psi_w(R_\alpha^{-1} \mathbf{r}'), \quad \phi(\mathbf{r}) \leftarrow \phi(R_\alpha^{-1} \mathbf{r}'). \quad (24)$$

Equations (13) and (15), together with the boundary conditions (20)–(22), are discretized on a two-dimensional spatial mesh. The equations are solved by using a multigrid method [22,23] with mesh spacings $\delta_x = 0.11$ and $\delta_z = 0.08$ on the finest grid. The details of the numerical method are given in the Appendix.

C. Charge-transfer rate and ion-neutralization probability

We describe the resonant charge-transfer process by the Schrödinger equation for the motion of the active electron in the collision plane of the projectile,

$$i\partial_t \Psi(t) = H \Psi(t), \quad H = T + V = -\frac{1}{2}(\partial_x^2 + \partial_z^2) + V(x, z), \quad (25)$$

where T is the kinetic energy of the electron and V is its potential energy as given in Eqs. (1), (3), and (17). The transition amplitude for charge transfer is calculated in adiabatic approximation for the motion of the ion, i.e., for an arbitrary but fixed ion position,

$$A(t; \mathbf{D}) = \langle \Psi(0) | \Psi(t; \mathbf{D}) \rangle, \quad (26)$$

where $|\Psi(0)\rangle$ is the initial unperturbed affinity state of H and \mathbf{D} is the position vector of the ion in the reference frame S . Information about the positions, widths, and amplitudes of resonances in the ion-surface system is contained in the projected density of states (PDOS),

$$\rho(E; \mathbf{D}) = \frac{1}{\pi} \text{Re} \int_0^\infty dt e^{iEt} A(t; \mathbf{D}). \quad (27)$$

The width Γ , position E_r , and amplitude a of an isolated resonance state are determined by fitting the PDOS to a Lorentzian curve and a constant background ρ_0 ,

$$\rho = \rho_0 + a \frac{\Gamma/2}{(E - E_r)^2 + \Gamma^2/4}. \quad (28)$$

In order to calculate the resonance parameters Γ , E_r , and a , we numerically integrate the Schrödinger equation (25) using the Crank-Nicholson propagation method on a single grid. The parameters of the numerical grid in this calculation are the same as in Ref. [7]. The grid extends over 100 equidistantly spaced atomic layers into the bulk with lattice constant a_0 and up to 100 a.u. into the vacuum side. The extension of the grid in the lateral direction is between $x = -400$ and $x = 400$. The grid spacings are $\Delta z = 0.2$ and $\Delta x = 0.3$, and the time step for the numerical propagation of the wave function is $\Delta t = 0.2$. The calculation of the PDOS was limited to distances $D \leq 11$ of the ion in front of the optical plane at $z = 0$, since at larger distances the wave function would have to be propagated over very long times ($> 15\,000$ a.u.) for the very narrow affinity-level resonance to become noticeable in the PDOS.

III. NUMERICAL RESULTS AND DISCUSSION

In this section we discuss our numerical results for the affinity-level width and ion-survival probability of H^- near both flat (Sec. III A) and vicinal (Sec. III B) surfaces. The purpose of Sec. III A is to assess the quantitative predictions and the limitations of our model.

A. Affinity-level width of H^- in front of flat jellium surfaces

In the jellium model for flat surfaces, the background charge density is $n_b \theta(-z)$. We numerically solved the one-dimensional version of Eqs. (13) and (15) for the grid size specified by $Z = 50$ and the mesh spacing $\delta_z = 0.05 r_s$, subject to the boundary conditions

$$\left(\frac{d\phi}{dz} \right)_{z=\pm Z} = 0, \quad \psi_w(-Z) = \sqrt{n_b}, \quad \psi_w(Z) = 0. \quad (29)$$

Figure 2 shows the normalized charge-density profiles $n = \psi_w^2/n_b$ and electrostatic Hartree potentials as a function of the distance z from the jellium edge in units of Fermi wavelengths. Table II shows good agreement of our results for the metallic work functions $W = -\mu$ calculated within the TFvW model for a collection of flat jellium surfaces with the data in [14], obtained within the same model, and the Lang-Kohn results [25,26].

The calculated PDOS in front of a Cu-like surface ($r_s \approx 3$) is shown in Fig. 3 for several positions D of the ion. At $D = 11.0$, the affinity level appears as a narrow Lorentzian peak far above the Fermi energy level E_F . At such large distances charge transfer is due to electron loss into unoccupied bulk states of the metal. Closer to the surface, at $D = 5.5$, the affinity energy level is shifted towards E_F . At $D = 3$ it becomes degenerate with the Fermi energy level ($E_a \approx E_F$), and the PDOS shows contributions evenly spread over the entire conduction band. For $D < 3$ the affinity energy level is shifted across and below the Fermi energy level, and the charge transfer reverses its direction to electron capture from the conduction band. Close to the jellium edge, at

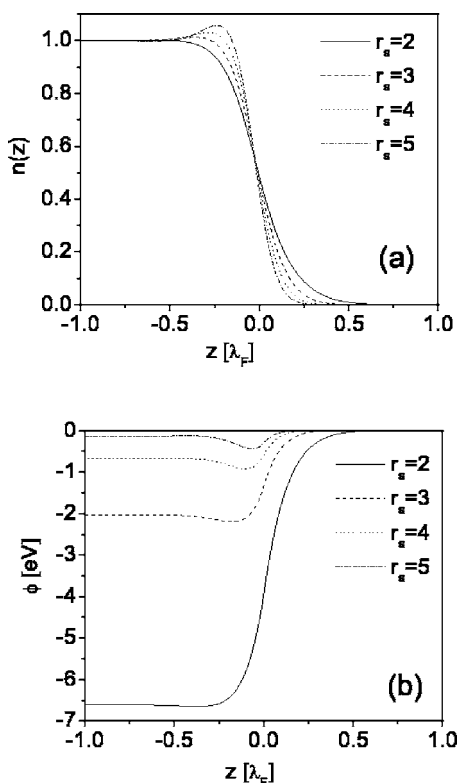


FIG. 2. Electronic charge densities (a), normalized to the bulk electronic density, and electrostatic potentials (b) for bulk Wigner-Seitz radii $r_s=2, 3, 4,$ and 5 . The distance z is measured in Fermi wavelengths (see Table I).

$D=1.0$, the resonance profile of the affinity level is truncated at the bottom of the conduction band.

Our model is based on the LDA for the effective exchange-correlation potential and excludes the image charge effects due to the long-range attractive interaction of the active electron with the induced polarization charge on the metal surface. In order to quantify the relevance of the image charge effect for electron transfer, we show in Fig. 4 the results of our calculations for the affinity level width of H^- near a flat Na surface with (xc) and without (x) correlation effects ($C_4=C_5=0$), in comparison with our results obtained from a model DFT potential [24], which includes the image charge effects. As this comparison suggests, our neglect of the image charge interaction leads to an increase of the charge-transfer rate of the order of 10%. Figure 4 also shows that neglecting correlation effects entails a reduction

TABLE II. Work functions W in eV for flat jellium surfaces, compared with calculations by Chizmishya and Zaremba [14] and Lang and Kohn [26].

r_s	Present result	Ref. [14]	Ref. [26]
2	3.70	3.70	3.89
3	3.22	3.22	3.50
4	2.83	2.84	3.06
5	2.53	2.55	2.73

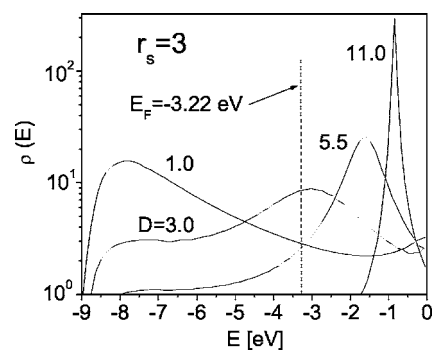


FIG. 3. Projected density of states in front of a Cu-like surface ($r_s=3$). The number above each curve refers to the position D of the ion with respect to the jellium edge.

of the affinity level width of the order of 20%–30% with respect to the DFT result.

Our affinity-level widths of the H^- near a flat Cu surface are plotted in Fig. 5 in comparison with results of Borisov *et al.* [6]. The calculations in [6] are based on the effective DFT potential [24], including the image charge effects. We have good quantitative agreement at smaller distances ($D < 4$); however, at intermediate and large distances our widths are 3–4 times larger. We attribute this disagreement to both the neglect of image forces and the reduced dimensionality of our model.

B. Neutralization of H^- in front of vicinal jellium surfaces

In this subsection we present numerical results for the charge-transfer rate and neutralization probability of H^- ions colliding with vicinal metallic surfaces at a kinetic energy of 1 keV. The static width of the projectile level is obtained from the PDOS given by Eq. (27). The ion-neutralization probabilities are evaluated within a rate-equation approach for a set of broken-straight-line trajectories, which reflect specularly depending on the local conditions at the metal-vacuum interface. The equilibrium electronic structure and the surface potentials were evaluated for bulk electron den-

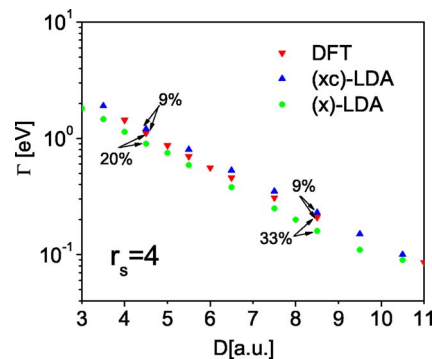


FIG. 4. (Color online) Affinity level widths of H^- as a function of the distance D from the jellium edge of a flat Na jellium surface ($r_s=4$). DFT: based on the effective potential of Ref. [24], which is adjusted to DFT results. (xc)-LDA: present result including exchange and correlation effects in local density approximation. (x)-LDA: present result excluding correlation effects.

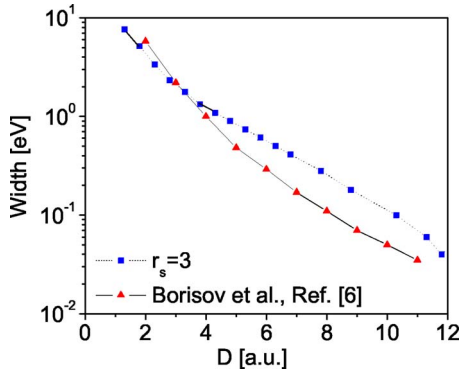


FIG. 5. (Color online) Comparison of the present result for the static widths of the affinity level of H^- in front of a Cu jellium surface ($r_s=3$) with the numerical data of Borisov *et al.* [6]. Distances are measured with respect to the image plane.

sities, corresponding to $r_s=2, 3$, and 4 (Table I).

Figure 6(a) shows the contour map of the normalized electron density ψ_w^2/n_b for a vicinal Al surface ($r_s=2$) with $(m,n)=(10,1)$. The lattice spacing for Al is $a_0=3.83$. The figure demonstrates the Smoluchowski effect of smoothing of the electron density near the step edges [27,28]. Electrons are effectively repelled from the step and flow from the edge into the valley between the upper and lower terraces. Near the edges, the electron density is highly nonuniform and this inhomogeneity spreads in a lateral direction over a distance of about one screening length. The electrons distribute similarly at the double-stepped vicinal Al surface with $(m,n)=(10,2)$, as shown in Fig. 6(b); however, the contour map follows more closely the jellium profile. Figure 6(c) presents the charge density of a vicinal Na surface ($r_s=4$) with $(m,n)=(10,2)$ and lattice spacing $a_0=3.99$. In comparison with Figs. 6(a) and 6(b), the electron distribution in Fig. 6(c)

is more extended in the lateral direction, due to the larger screening length of Na as compared to Al. Inside the bulk, the charge-density overshoot, which is driven by the gradient-correction term in Eq. (5), is modulated due to the presence of steps. The electrostatic potentials in Figs. 6(d)–6(f) correspond to the electron densities in Figs. 6(a)–6(c). Due to the electron depletion from the step edges, a residual unscreened electrostatic field of the edge ionic cores penetrates into the vacuum side of the interface, while the equipotential lines bend towards the lower corner of the step due to the electron density increase in this domain.

The redistribution of the electron density at steps induces a dipole moment, which is oriented towards vacuum [Figs. 6(a)–6(c)]. As shown in [29], the step dipole due to this redistribution slightly diminishes the dipole moment on the flat terrace and thus leads to a decrease of the metallic work function W relative to the work function of a flat surface, W_{flat} . Table III displays our results for the work function change $\Delta W=W_{\text{flat}}-W$ in comparison with the theoretical data of Ishida and Liebsch [29] and work-function changes measured by Roth *et al.* [30] for the Cu(117) and Cu(119) vicinal surfaces of the flat Cu(001) surface. We note that the work-function change for surfaces with step height $2a_0$ is larger than for surfaces with step height a_0 , due to the increased dipole moment along the step edge.

Our results for ΔW agree well with both theoretical values based on the Kohn-Sham approach [29] and the experimental data for vicinal Cu(117) and Cu(119) surfaces [30]. This provides evidence for a realistic description of the electronic density distribution at the metal-vacuum interface within the TFvW method.

The self-consistent electron-surface interaction potentials in Fig. 7 show steep gradients near the step edges and vary more slowly towards the lower corner of the step, due to the above-mentioned electron density redistribution. The importance of the gradient correction term in Eq. (5) and

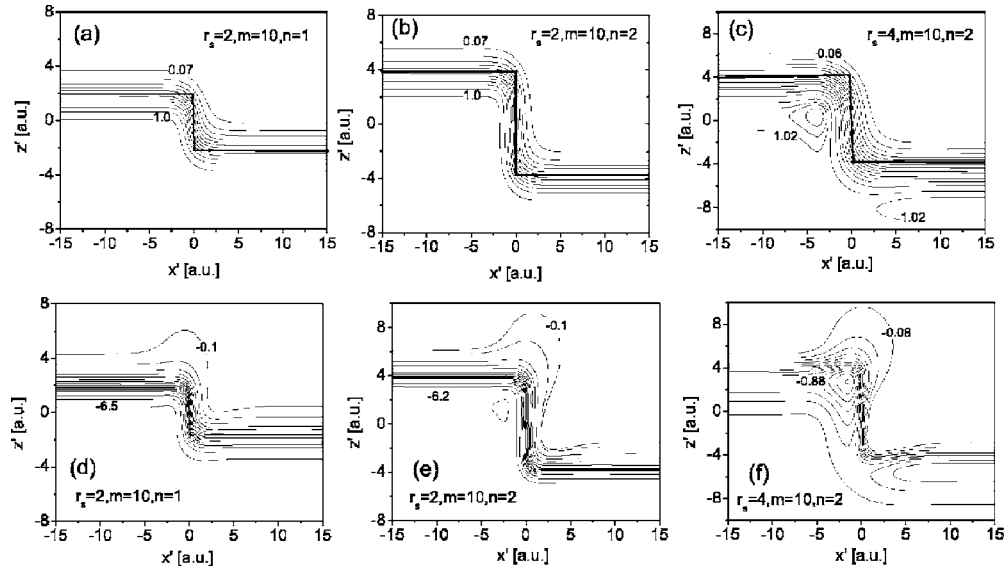


FIG. 6. Contour maps of the normalized electron charge densities $n(x', z')/n_b$ (a)–(c) and electrostatic potentials $\phi(x', z')$ (d)–(f) for vicinal Al ($r_s=2$) (a), (b), (d), (e) and Na ($r_s=4$) (c), (f) surfaces with step length $10a_0$ and step heights a_0 (a), (d) and $2a_0$ (b), (c), (e), (f). The solid line in (a)–(c) indicates the profile of the positive ionic background charge. The contour-line spacing is 0.07 (a), (b), 0.08 (c), 0.43 eV (d), 0.44 eV (e), and 0.08 eV (f). The lattice spacings are $a_0=3.99$ for Na and $a_0=3.83$ for Al.

TABLE III. Calculated work function W and work function change ΔW in eV compared with results based on the Kohn-Sham equations [29] and experimental data for vicinal Cu(117) and Cu(119) surfaces [30]. The first column presents the value of the screening parameter r_s , the second and third columns specify the surface morphology (m, n) , the fourth and fifth column show our results, and the last row includes published data for ΔW .

r_s	m	n	This work		Literature data
			W	ΔW	ΔW
2	10	1	3.66	0.03	0.03 [29]
2	10	2	3.63	0.07	0.05 [29]
2.7	8	1	3.30	0.05	0.03 [30] for Cu(117) 0.04 [30] for Cu(119)
2.7	8	2	3.26	0.09	
3	10	2	3.16	0.06	
4	10	2	2.75	0.08	

exchange-correlation effects is also expressed in the appearance of a local minimum in the Na surface potential, as indicated by the closed contour line in the metal interior in Fig. 7(c).

The PDOS of the system is calculated for a sequence of lateral positions D_{par} of the ion at a fixed distance D_{nor} in front of the optical surface as indicated in Fig. 8. The PDOS for a vicinal Al surface with $(m, n) = (10, 1)$ is shown in Fig. 9(a) for $D_{\text{nor}} = 4$. At the midterrace position (3), at $D_{\text{par}} = 8$, the affinity level lies above the Fermi energy level ($E_F = -3.66$ eV) and charge transfer is due to electron loss. The width of the affinity level resonance is $\Gamma = 1.34$ eV. When positioned above the lower corner of the step [position (2), $D_{\text{par}} = 2$], the affinity energy level is shifted close to E_F and the resonance width becomes $\Gamma = 2.16$ eV. Right above the step edge [position (1), $D_{\text{par}} = -2$], where affinity is below E_F , the width is very large ($\Gamma \approx 4.68$ eV) and the charge transfer proceeds via electron capture from the delocalized bulk states of the target. At larger distances from the optical surface plane, at $D_{\text{nor}} = 7$, the PDOS lies to a great extent above E_F , as shown in Fig. 9(b); i.e., the transfer is due to electron loss. The affinity-level width is now 1.07, 0.77, and 0.50 eV at positions (1), (2), and (3), respectively. The abrupt variation of the width in the vicinity of the step edge [position (1)] can be explained in terms of the width of the potential barrier between the surface and projectile [cf. Fig. 7(a)]. At the upper corner of the step, the surface potential rises steeply toward the vacuum. This reduces the barrier width and favors electron tunneling, while electron transfer near the lower corner of the step is less likely, due to the larger barrier width.

Figure 10 shows the PDOS in front of a double-stepped vicinal Na surface ($r_s = 4$) with $(m, n) = (10, 2)$, for two positions of the H⁻ ion in front of the optical plane, $D_{\text{nor}} = 5$ and 8, respectively. The Fermi energy level is at $E_F = -2.75$ eV. The charge-transfer process shares qualitatively the same features as discussed above for the monoatomic vicinal Al; however, the affinity level shift and width vary more rapidly with the lateral coordinate D_{par} . At $D_{\text{nor}} = 5$, the charge trans-

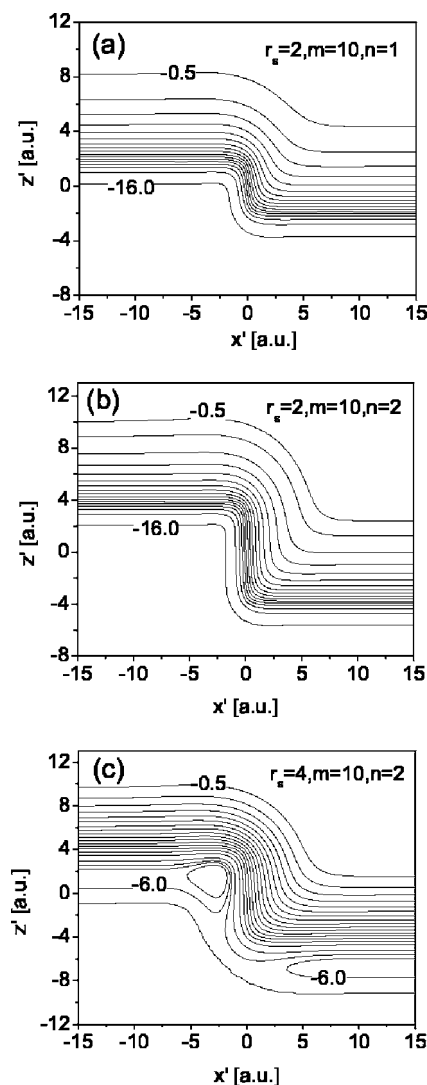


FIG. 7. Electron-surface interaction potentials according to Eq. (17) for vicinal Al ($r_s=2$) with step heights a_0 (a) and $2a_0$ (b) and for vicinal Na ($r_s=4$) with step height $2a_0$ (c). The step length is $10a_0$ in all graphs. $a_0=3.83$ for Al and $a_0=3.99$ for Na. The contour-line spacing is 1 eV (a), (b) and 0.3 eV (c).

fer results in electron loss near the midterrace position (3), the affinity becomes degenerate with E_F ($E_a \approx E_F$) near the lower corner of step (2) [Fig. 10(a)]. The effect of the narrower conduction band of Na is seen in the saturation of the width near the upper corner of the step at position (1), where the energy level is shifted close to the bottom of the conduction band, $E_b \approx -6$ eV. At position (1) the width is 1.33 eV, at the lower corner position (2) we have 1.46 eV, and at the midterrace position (3) $\Gamma = 0.45$ eV. At $D_{\text{nor}} = 8$, in Fig. 10(b), the loss process determines the character of the charge transfer and the width shows a larger variation with D_{par} as compared to the monoatomically stepped vicinal Al. Above the step edge at position (1), the width is $\Gamma = 1.00$ eV, while at the midterrace position (3) we find $\Gamma = 0.17$ eV.

The static widths extracted from the PDOS for the vicinal Al surface with $(m, n) = (10, 1)$ and $(m, n) = (10, 2)$ and Na surface with $(m, n) = (10, 2)$ are shown in Figs. 11(a)–11(c), respectively. We find that the affinity level width Γ clearly

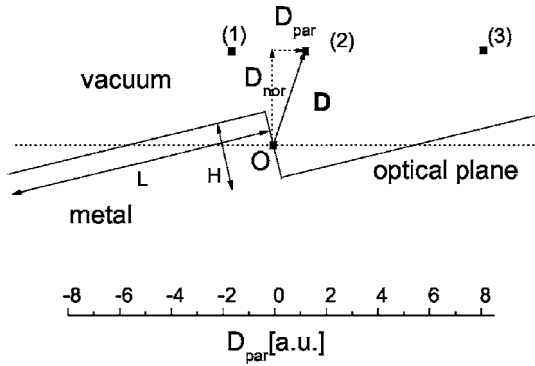


FIG. 8. Geometry for the calculation of the PDOS of H^- in front of a vicinal surface. The ion position vector $\mathbf{D}=(D_{\text{par}}, D_{\text{nor}})$ is measured with respect to the origin O of the reference frame S in the Fig. 1. Position (1) of the ion is near the upper corner of the step, position (2) is above the lower corner of the step, and point (3) is above the midterrace position.

exhibits the vicinal structure of the surface. It oscillates in the lateral direction with the terrace period and decays exponentially into the vacuum. The charge transfer results in electron loss near midterrace positions, where Γ acquires a minimum. For small distances $D_{\text{nor}} \approx 4$ and near the step edges, the affinity level is shifted across and below the Fermi level and charge transfer proceeds by capture of a target electron from the conduction band. The effect of the narrower conduction band of Na is expressed in the sudden decrease of

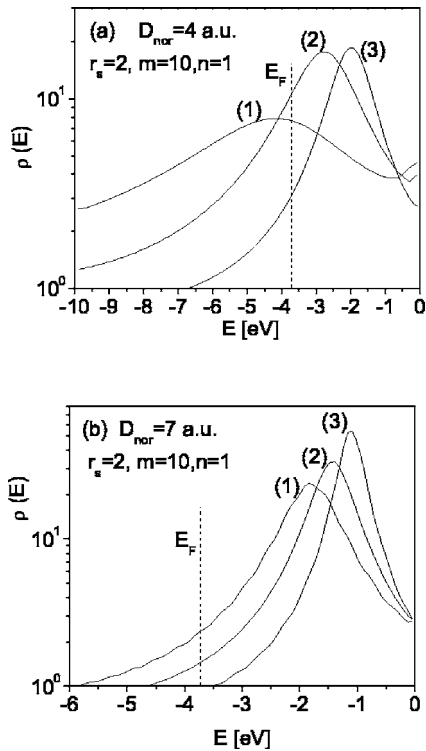


FIG. 9. Projected density of states for H^- in front of a vicinal Al surface with $(m,n)=(10,1)$. The ion is at $D_{\text{nor}}=4.0$ a.u. in front of the optical plane (a) and at $D_{\text{nor}}=7.0$ a.u. (b). The lateral positions of the ion, (1), (2), and (3), are indicated in Fig. 8. The Fermi level $E_F=-3.66$ eV is denoted with a dotted line.

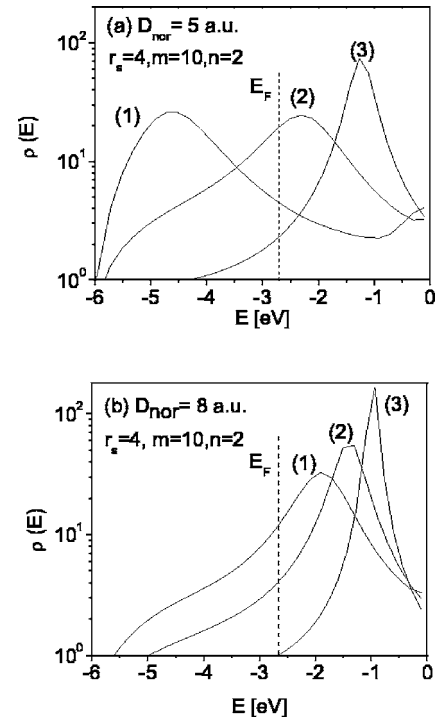


FIG. 10. Projected density of states for H^- in front of a vicinal Na surface with $(m,n)=(10,2)$. The ion is at $D_{\text{nor}}=5.0$ a.u. in front of the optical plane (a) and at $D_{\text{nor}}=8.0$ a.u. (b). The lateral positions of the ion, (1), (2), and (3), are indicated in Fig. 8. The Fermi level $E_F=-2.75$ eV is denoted with a dotted line.

the width at small D_{nor} in the vicinity of the step edges [cf. Fig. 11(c)].

The survival probability P of H^- in collisions with a vicinal Al surface with $(m,n)=(10,1)$ is calculated from the rate equation

$$\frac{dP}{dt} = -\Gamma_{\text{loss}}(t)P + \Gamma_{\text{cap}}(t)(1-P), \quad (30)$$

where Γ_{loss} and Γ_{cap} are the electron loss and capture rates evaluated along the projectile's trajectory $\mathbf{D}(t)$. We assume the following description for the ion-neutralization process: if the affinity level E_a is above the Fermi energy level, the ion is neutralized via electron loss, while below E_F only capture is allowed—i.e.,

$$\Gamma_{\text{loss}} = \begin{cases} \Gamma, & E_a \geq E_F, \\ 0, & E_a < E_F, \end{cases} \quad \Gamma_{\text{cap}} = \begin{cases} 0, & E_a \geq E_F, \\ \Gamma, & E_a < E_F. \end{cases} \quad (31)$$

Due to the broken translational invariance of the interface in the lateral direction, the ion-survival probability depends on the local surface conditions. The rate equation (30) is solved for a set of predefined straight-line trajectories, which reflect specularly on the terrace at the point of closest approach D_{cls} and at a fixed distance D_{step} from the step ledge. We consider only two types of collision trajectories. Trajectories which approach the step ledge from above will be referred to as “step-down” and those approaching the ledge from below as “step-up.” These trajectories are sketched in

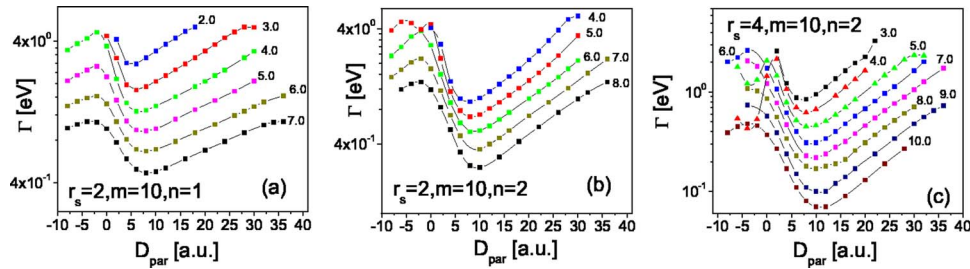


FIG. 11. (Color online) Static affinity-level width of H^- as a function of the ion position ($D_{\text{par}}, D_{\text{nor}}$) in front of a vicinal Al surface ($r_s=2$) with $(m,n)=(10,1)$ (a), vicinal Al surface ($r_s=2$) with $(m,n)=(10,2)$ (b), and vicinal Na surface ($r_s=4$) with $(m,n)=(10,2)$ (c). The numbers attached to each curve indicate the distance D_{nor} (in a.u.) of the ion from the optical surface plane.

Fig. 12. Trajectories which are significantly perturbed by the steps are not considered.

Figure 12(a) shows the survival probability of the ion along step-up and step-down trajectories as a function of the angle of incidence with respect to the optical surface plane. The ion reflects specularly at a distance $D_{\text{step}}=3a_0$ from the step ledge and point of closest approach $D_{\text{cls}}=1.0$ above or below the step. We see that the ion-survival probability is a rapidly varying function of the incidence angle θ_{inc} and that survival along step-down trajectories is more likely. Moreover, the survival probability along the step-up trajectories has a well-pronounced resonance dip at an incidence angle of about 25° . The survival along step-down trajectory also shows a small dip at $\theta_{\text{inc}} \approx 15^\circ$. A similar qualitative behavior of the survival probability is observed if the ion reflects near a midterrace position at the distance $D_{\text{step}}=5a_0$ from the ledge, as seen in Fig. 12(b). The dip in the ion-survival probability along the step-up trajectory is shifted to smaller angles of incidence, close to $\theta_{\text{inc}} \approx 18^\circ$. The survival along the step-down trajectory is more likely and monotonically decreases with the decrease of the incidence angle.

In order to further analyze these results, we show the variation of the affinity energy level E_a along the projectile's trajectory for reflection at $D_{\text{step}}=3a_0$ above or below the step (Fig. 13). At large angles of incidence the survival probability is large $P \approx 10\%$, since the interaction time of the projectile with the surface is minimal. The affinity level depends only weakly on details of the surface morphology [Figs.

13(a)–13(d)]. The survival probability for a step-up trajectory at $\theta_{\text{inc}}=26^\circ$ is $P \approx 0.1\%$ [Figs. 13(e) and 12(a)]. This is due to an increase of the interaction time and enhancement of the electron loss at the nearest step edge on the outgoing part of the trajectory, after E_a has crossed E_F from below. By further decreasing the angle of incidence to $\theta_{\text{inc}}=20^\circ$ [Fig. 13(g)], the affinity level of the projectile repeatedly crosses the Fermi energy level after reflection from step-up trajectory. On the exit part of this trajectory, at the position of the nearest step edge, the electron transfer occurs via capture from the conduction band ($E_a < E_F$), which indeed favors ion survival, $P \approx 1\%$. We conclude that the dip in the survival probability along the step-up trajectory is due to resonant enhancement of the electron loss on the outgoing part of the scattering trajectory, caused by the presence of a perturbing step edge on the surface. Ion survival along the step-down trajectories is favored, since the projectile is reflected away from the nearest step edge, which decreases the interaction time [Figs. 13(b), 13(d), and 13(f)]. However, at smaller angles of incidence, for $\theta_{\text{inc}}=12^\circ$, electron loss is enhanced along the incoming part of the step-down trajectory, due to the encounter of an edge prior to reflection from a terrace [Fig. 13(h)].

Our conclusions in this paper agree qualitatively with earlier results of a theoretical study on the formation of H^- ions at stepped Al surfaces in grazing incidence collisions [31], which clearly reveal enhancement of the ion-formation probability along step-down trajectories. We also note that the

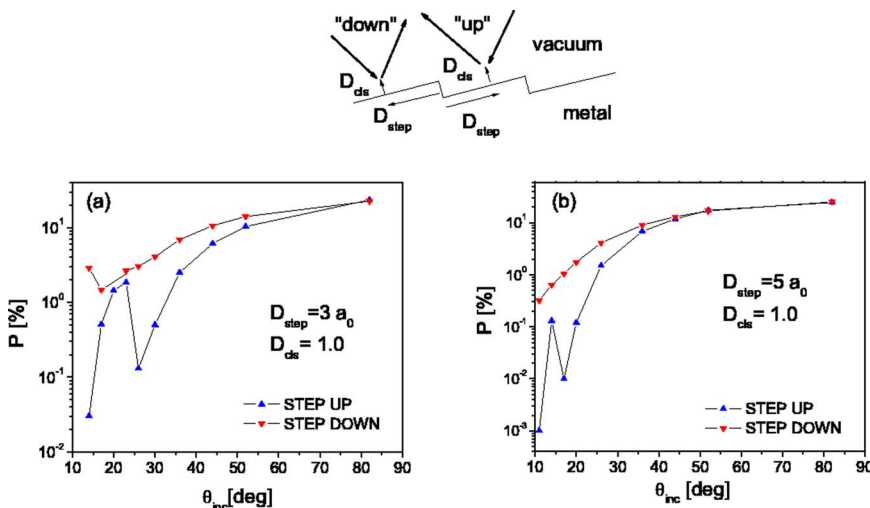


FIG. 12. (Color online) Ion-survival probability for 1 keV H^- colliding with a monoatomic vicinal Al surface ($n=1$) as a function of the projectile's angle of incidence θ_{inc} with respect to the optical surface plane. The ion reflects specularly at the point of closest approach $D_{\text{cls}}=1.0$ a.u. above the upper terrace (step-down) or lower terrace (step-up) at a distance $D_{\text{step}}=3a_0$ (a) or $5a_0$ (b) from the step ledge. The crystal lattice spacing is $a_0=3.83$ a.u. and the terrace width is $L=10a_0$.

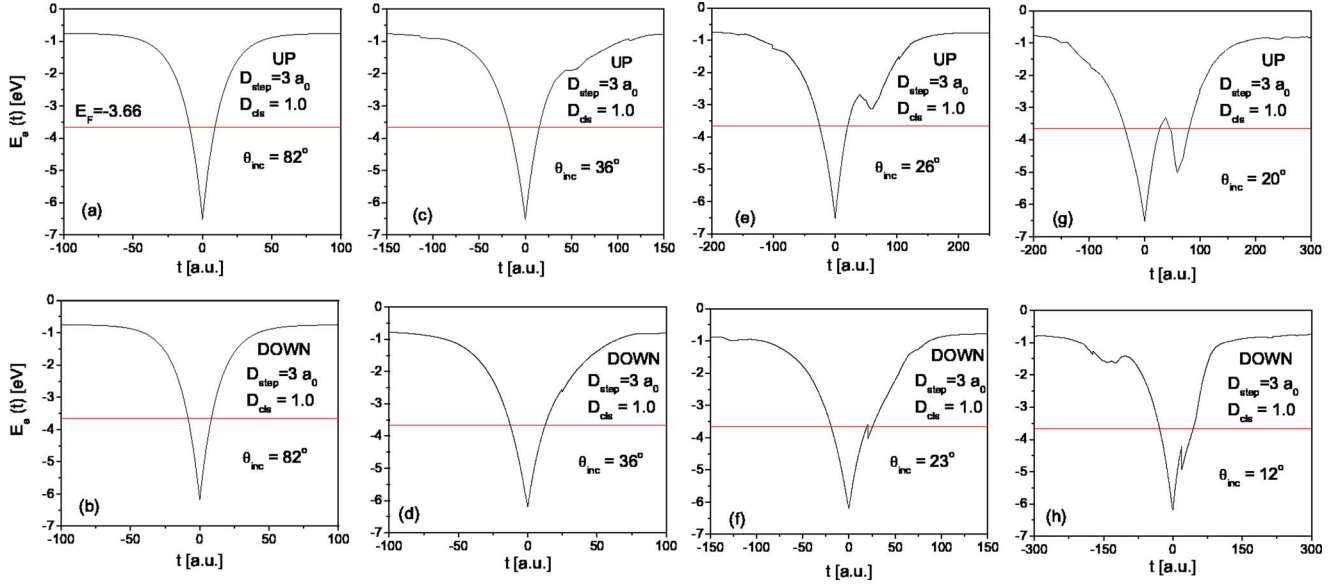


FIG. 13. (Color online) Affinity energy level of H^- along the projectile's trajectory at a kinetic energy $E=1$ keV colliding with vicinal Al surface ($m=10, n=1$). θ_{inc} is the angle of incidence with respect to the optical surface plane. The distance of closest approach is $D_{cls}=1.0$ and the distance from the step ledge is $3a_0$. (a) Step-up trajectory, $\theta_{inc}=82^\circ$. (b) Step-down trajectory, $\theta_{inc}=82^\circ$. (c) Step-up trajectory, $\theta_{inc}=36^\circ$. (d) Step-down trajectory, $\theta_{inc}=36^\circ$. (e) Step-up trajectory, $\theta_{inc}=26^\circ$. (f) Step-down trajectory, $\theta_{inc}=23^\circ$. (g) Step-up trajectory, $\theta_{inc}=20^\circ$. (h) Step-down trajectory, $\theta_{inc}=12^\circ$.

oscillations of the affinity-level width, shown in Fig. 13, are consistent with both the result of LDA calculations based on a cluster model for the surface [32] and scattering experiments with 4-keV Ne^+ ions on vicinal CdS surfaces. In Ref. [12], a clear correlation has been observed between the Ne^+ fractions and the lateral variation of the surface potential along the outgoing trajectories of the scattered ions. The authors observe an increased neutralization probability near Cd atoms, due to the depletion of electronic charge near these atoms, and decreased neutralization near S atoms, due to the increase of electron density around the sulfur atoms.

IV. CONCLUSION AND OUTLOOK

We have calculated the neutralization probability of H^- ions colliding with vicinal surfaces at a kinetic energy of 1 keV. The surface electronic structure is calculated within an application of the Thomas–Fermi–von Weizsäcker model using a local density approximation for the exchange and correlation energy [14]. Our results for the work function change near vicinal metal surfaces are in good agreement with both experiment [30] and Kohn-Sham calculations [29] and indicate that we represent the metal-vacuum interface fairly accurately. The presence of localized dipole moments at steps predicted within the TFvW model is consistent with recent experimental measurements [28]. The affinity-level width of H^- as a function of the ion-surface distance is obtained by projecting the density of states of the collision system onto the unperturbed projectile affinity level. We find a resonant enhancement of the electron loss along the outgoing part of the projectile's trajectory, depending on the direction of the surface steps. As a consequence we find that ion survival is less likely along step-up trajectories. Our conclu-

sions in this work are also consistent with the predicted increase of the H^- formation probability in grazing collisions with Al surfaces along step-down trajectories [31].

Our jellium-based approach does not include the periodic crystal structure of the metal in the bulk or the contribution from the long-range image forces. We will extend our model by including these effects in the future. In parallel, we intend to improve our modeling of the classical motion of the projectile, in response to the sensitive dependence of the ion-survival probability on the collision trajectory predicted in this work.

ACKNOWLEDGMENTS

This work was supported by NSF Grant No. PHY03548400 and by the Chemical Sciences, Geosciences, and Biosciences Division, Office of Basic Energy Sciences, Office of Science, U.S. Department of Energy.

APPENDIX: SOME DETAILS OF THE NUMERICAL METHOD

Due to the translational invariance of the jellium system in the step-edge direction, Eqs. (13) and (15) together with boundary conditions (20)–(22) are discretized on a two-dimensional spatial mesh $\Omega^h=(\delta_x, \delta_z)$, with standard central finite-difference approximation for the Laplacian. The nonlinear Schrödinger equation (15) is solved by iteration in imaginary time,

$$\psi^h(t + \delta t) = \psi^h(t) + \left(-\frac{\lambda_w}{2} L^h + v_{eff}^h - \mu \right) \psi^h(t) \delta t, \quad (A1)$$

where L^h is the finite-difference approximation for the Laplacian and the parameter δt satisfies the stability condition

$\delta t < (1/4) \min(\delta_x^2, \delta_z^2)$. First, a trial density is defined and the electrostatic potential is evaluated from the Poisson's equation with multigrid method [22,23]. ϕ^h and $\bar{\phi}^h$ are the exact and approximate solution on the finest grid. The residual of Poisson's equation is $r^h = f^h - L^h \bar{\phi}^h$ with $f^h = -4\pi(\psi^2 - n_i)$. The error $e^h = \phi^h - \bar{\phi}^h$ also satisfies Poisson's equation $L^h e^h = r^h$. The residual is transferred to a coarser grid (with $H = 2h$), $r^H = I_h^H r^h$, where I_h^H is a linear restriction operator, which evaluates the residual on the coarser grid by taking a local average of the fine-grid residual. The residual equation $L^H e^H = r^H$ on the coarser grid is solved, and the fine-grid approximation is updated via $\bar{\phi}^h \leftarrow \bar{\phi}^h + I_H^h e^H$, where I_H^h is a linear interpolation operator from the coarse to the fine grid. In order to accelerate the convergence properties of this coarse grid correction scheme, the number of the coarser grids is successively increased ($\Omega^h, \Omega^{2h}, \Omega^{4h}, \dots$), and the two-grid iteration is applied sequentially between these grids, proceeding from the finest to the coarsest and back to the finest grid. This cycle is repeated N_v times at each level of refinement. This is necessary in order to accelerate the damping of the low-frequency error components of the correction to the solution on the finest grid, while the high-frequency components of the error are smoothed by using a

relaxation method applied ν_1 times in the beginning of the coarse grid correction and ν_2 times at the end.

We use a bilinear interpolation for the operator I_H^h , a half-weighting scheme for the restriction operator I_h^H , and use Gauss-Seidel relaxation for the solution update process, by sequentially relaxing the residual equation on the grid lines for fixed x . At each iteration step we Gram-Schmidt normalize the solution to the right-hand side of the Poisson's equation, as required by the Neumann boundary conditions (20) and (22). We use six grids in the numerical calculation of the electrostatic potential. Mesh spacings on the finest grid $\delta_x = 0.11$ and $\delta_z = 0.08$ were found to be adequate. The convergence properties and the quality of the solution were assessed empirically by monitoring the L_2 norm of the residual on the finest grid. For $\nu_1 = \nu_2 = 5$ and $N_v = 15$, we find that the relaxation scheme approximates the electrostatic potential sufficiently well.

The electrostatic potential ϕ is used to update the effective potential v_{eff} in Eq. (16) and the value of the chemical potential in Eq. (14). The new approximation for the von Weizsäcker wave function is obtained from Eq. (A1). The iterations proceed until self-consistency is reached. The self-consistency is assumed when the chemical potential has converged to six significant digits.

-
- [1] M. Maazouz, A. G. Borisov, V. A. Esaulov, J. P. Gauyacq, L. Guillemot, S. Lacombe, and D. Teillet-Billy, Phys. Rev. B **55**, 13 869 (1997).
- [2] L. Guillemot and V. A. Esaulov, Phys. Rev. Lett. **82**, 4552 (1999).
- [3] P. Nordlander and J. C. Tully, Phys. Rev. Lett. **61**, 990 (1998).
- [4] J. Burgdörfer, in *Review of Fundamental Processes and Applications of Atoms and Ions*, edited by C. D. Lin (World Scientific, Singapore, 1993).
- [5] P. Kürpick and U. Thumm, Phys. Rev. A **58**, 2174 (1998).
- [6] A. G. Borisov, A. K. Kazansky, and J. P. Gauyacq, Phys. Rev. B **59**, 10935 (1999).
- [7] H. Chakraborty, T. Niederhausen, and U. Thumm, Phys. Rev. A **70**, 052903 (2004).
- [8] P. Nordlander and N. D. Lang, Phys. Rev. B **44**, 13 681 (1991).
- [9] A. Murgaza, A. Mascaraque, V. Pérez-Dieste, V. Repain, S. Rousset, F. J. García de Abajo, and J. E. Ortega, Phys. Rev. Lett. **87**, 107601 (2001).
- [10] F. Schiller, M. Ruiz-Osés, J. Cerdón, and J. E. Ortega, Phys. Rev. Lett. **95**, 066805 (2005).
- [11] C. C. Hsu, H. Bu, A. Bousetta, J. W. Rabalais, and P. Nordlander, Phys. Rev. Lett. **69**, 188 (1992).
- [12] L. Houssiau, J. W. Rabalais, J. Wolfgang, and P. Nordlander, Phys. Rev. Lett. **81**, 5153 (1998).
- [13] C. A. Utreras-Diaz, Phys. Rev. B **36**, 1785 (1987).
- [14] A. Chizmeshya and E. Zaremba, Phys. Rev. B **37**, 2805 (1988).
- [15] R. Brako and D. M. Newns, Rep. Prog. Phys. **52**, 665 (1989).
- [16] J. Los and J. J. C. Geerlings, Phys. Rep. **190**, 133 (1990).
- [17] J. S. Cohen and G. Fiorentini, Phys. Rev. A **33**, 1590 (1986).
- [18] V. A. Ermoshin and A. K. Kazansky, Phys. Lett. A **218**, 99 (1996).
- [19] D. A. Kirzhnits, Sov. Phys. JETP **5**, 64 (1957).
- [20] W. Kohn and L. J. Sham, Phys. Rev. **140**, A1133 (1965).
- [21] B. Lang, R. W. Joyner, and G. A. Somorjai, Surf. Sci. **30**, 440 (1970).
- [22] W. H. Press, S. A. Teukolsky, W. T. Vetterling, and B. P. Flannery, *Numerical Recipes in FORTRAN* (Cambridge University Press, Cambridge, England, 1993).
- [23] A. Brandt, in *Multigrid methods, Proceedings of the Conference Held at Köln-Porz, 1981*, edited by W. Hackbusch and U. Trottenberg (Springer-Verlag, Berlin, 1982), p. 220.
- [24] P. J. Jennings, R. O. Jones, and M. Weinert, Phys. Rev. B **37**, 6113 (1998).
- [25] N. D. Lang and W. Kohn, Phys. Rev. B **1**, 4555 (1970).
- [26] N. D. Lang and W. Kohn, Phys. Rev. B **3**, 1215 (1971).
- [27] R. Smoluchowski, Phys. Rev. **60**, 661 (1941).
- [28] J. Y. Park, G. M. Sacha, M. Enachescu, D. F. Ogletree, R. A. Ribeiro, P. C. Canfield, C. J. Jenks, P. A. Thiel, J. J. Sáenz, and M. Salmeron, Phys. Rev. Lett. **95**, 136802 (2005).
- [29] H. Ishida and A. Liebsch, Phys. Rev. B **46**, 7153 (1992).
- [30] M. Roth, M. Pickel, J. Wang, M. Weinelt, and Th. Fauster, Appl. Phys. B: Lasers Opt. **74**, 661 (2002).
- [31] G. E. Makhmetov, A. G. Borisov, D. Teillet-Billy, and J. P. Gauyacq, Surf. Sci. **366**, L769 (1996).
- [32] M. Taylor and P. Nordlander, Phys. Rev. B **64**, 115422 (2001).